Impact of grids and dynamical cores in CESM2.2 on the meteorology and climate of the Arctic

Adam R. Herrington [1], Marcus Lofverstrom [2], Peter H. Lauritzen [1] and Andrew Gettelman [1]

[1]National Center for Atmospheric Research, 1850 Table Mesa Drive, Boulder, Colorado, USA
[2]Department of Geosciences, University of Arizona, 1040 E. 4th Street, Tucson, AZ USA

Key Points:

- enter point 1 here
- enter point 2 here
- enter point 3 here

Corresponding author: =name=, `=email address=`

Abstract

[enter your Abstract here]

Plain Language Summary

[enter your Plain Language Summary here or delete this section]

1 Introduction

General Circulation Models (GCMs) are powerful tools for understanding the meteorology and climate of the high-latitudes, which are among the most sensitive regions on Earth to global and environmental change. Despite their importance, the numerical treatment of polar regions in GCMs is handled in vastly-different ways due to the so-called *pole-problem* (D. Williamson, 2007), which refers to numerical instability arising from the convergence of meridians at the polar points on latitude-longitude grids (e.g., Figure 1a). Depending on the numerics, methods exist to suppress this instability, and latitude-longitude grids may be advantageous for polar processes as structures can be represented with more degrees of freedom than elsewhere in the computational domain. With the recent trend towards globally uniform unstructured grids, any potential benefits of latitude-longitude grids on polar regions may become a relic of the past. In this study, a spectrum of model grids and dynamical cores (hereafter referred to as *dycores*) available in the Community Earth System Model, version 2.2 (CESM; `http://www.cesm.ucar.edu/models/cesm2/`) are evaluated to understand their impacts on the simulated characteristics of the Arctic, with a special focus on the meteorology over the Greenland Ice Sheet.

In the 1970's the pole problem was largely defeated through wide-spread adoption of efficient spectral transform methods in GCMs. These methods transform grid point fields into a global, isotropic representation in wave space, where linear operators (e.g. horizontal derivatives) in the equation set can be solved for exactly. While spectral transform methods are still used in the 21st century, local numerical methods have become desirable for their ability to run efficiently on massively parallel systems. The pole-problem has thus re-emerged in contemporary climate models that use latitude-longitude grids, and some combination of reduced grids and polar filters are necessary to ameliorate this instability (Jablonowski & Williamson, 2011). Polar filters are akin to a band-aid; they subdue the growth of unstable modes by applying additional damping to the solution over polar regions. One might expect that this additional damping reduces the effective resolution such that the resolved scales are similar across the entire domain, but this seems unlikely (describe why) and is explored further in this study.

An alternative approach is to use unstructured grids, which allow for more flexible grid structures that permit quasi-uniform grid spacing globally and eliminates the pole-problem entirely (e.g., Figure 1c). This grid flexibility also allows for variable-resolution or regional grid refinement (e.g., Figure 2). Grids can be developed with refinement over polar regions that could in principle make up for any loss in polar resolution in transitioning away from latitude-longitude grids (e.g., Figure 2), although this comes at the cost of a smaller CFL-limiting time-step in the refined region (the CFL-condition — short for Courant–Friedrichs–Lewy condition — is a necessary condition for numerical stability when using discrete data in time and space). However, unstructured grids scale more efficiently on parallel systems than latitude-longitude grids, likely resulting in a greater prevalence of unstructured grids as computing power continued to increase over time.

The meteorology and climate of the Arctic is characterized by a range of processes and scales that are difficult to represent in GCMs (Bromwich et al., 2001; Smirnova & Golubkin, 2017; van Kampenhout et al., 2018). For example, while synoptic scale storms are generally well represented at typical GCM resolutions of 1 to 2 degrees (Jablonowski & Williamson, 2006; Stocker, 2014), mesoscale Polar Lows are not well resolved at these resolutions. These mesoscale systems are prevalent during the cold season and produce gale-force winds that can induce large heat and moisture fluxes through the underlying sea-ice/ocean interface. The Arctic also contains the Greenland Ice Sheet (hereafter denoted as *GrIS*). While it blankets the largest island in the world (Greenland), many of the processes that control the GrIS annual surface mass balance (the integrated sum of precipitation and melting) are only partially resolved at typical GCM resolutions. For example, GrIS precipitation is typically confined to the ice-sheet margins (predominately the southeastern margin) where orographic precipitation is generated by steep topographic slopes. Moreover, GrIS ablation areas (marginal regions where seasonal melting exceeds the annual mass input from precipitation) are typically 10s to 100 km wide and confined to low-level areas or regions with limited precipitation. GCMs struggle to resolve the magnitude and extent of these features (van Kampenhout et al., 2018), which can lead to unrealistic ice sheet growth in models with an interactive ice sheet component (e.g., Lofverstrom et al., 2020).

The goal of this study is to characterize the representation of high-latitude regions using the spectral-element and finite-volume dycores in CESM2.2, as these models treat the high-latitudes, e.g., the pole-problem, in different ways. The manuscript is laid out as follows: Section 2 consists of documentation of the grids, dycores and physical parameterizations used in this study. The Arctic refined grids were developed by the authors, and this section serves as their official documentation in CESM2.2. Section 2 also contains a description of the experiments along with reanalysis datasets and post-processing software used for evaluating the model simulations. Section 3 contains the results of the experiments, followed by Section 4 that provides a general discussion and conclusions.

2 Methods

2.1 Dynamical cores

The atmospheric component of CESM2.2, the Community Atmosphere Model, version 6.3 (CAM; `https://ncar.github.io/CAM/doc/build/html/index.html`), supports a number of different atmospheric dynamical cores. These include dycores using latitude-longitude grids, such as finite-volume (FV; Lin, 2004) and eulerian spectral transform (EUL; Collins et al., 2006) models, and dycores built on unstructured grids, including spectral-element (SE; Lauritzen et al., 2018) and finite-volume 3 (FV3; Putman & Lin, 2007) models. The EUL dycore is the oldest dycore in CAM, and the least supported of all the dycores in the current model. FV3 is the newest dycore in CAM, but it was not fully incorporated at the time this work commenced; both the EUL and FV3 dycores are omitted from this study. As such, the results presented in this study are comparing the performance of the SE and FV dycores.

2.1.1 Finite-volume (FV) dynamical core

The FV dycore is a hydrostatic model that integrates the equations of motion using a finite-volume discretization on a spherical latitude-longitude grid (Lin & Rood, 1997). The 2D dynamics evolve in floating Lagrangian layers that are periodically mapped to Eulerian reference grid in the vertical (Lin, 2004), using a hybrid-pressure vertical coordinate. Hyperviscous damping is applied to the divergent modes while Laplacian damping is applied to momentum in the top few layers, referred to as a *sponge layer* (Lauritzen et al., 2011). A polar filter is used to avoid computational instability due to the convergence of the meridians, allowing for a more practical time-step. It takes the form of a Fourier filter in the zonal direction, with the damping coefficients increasing monotonically in the poleward direction (Suarez & Takacs, 1995).

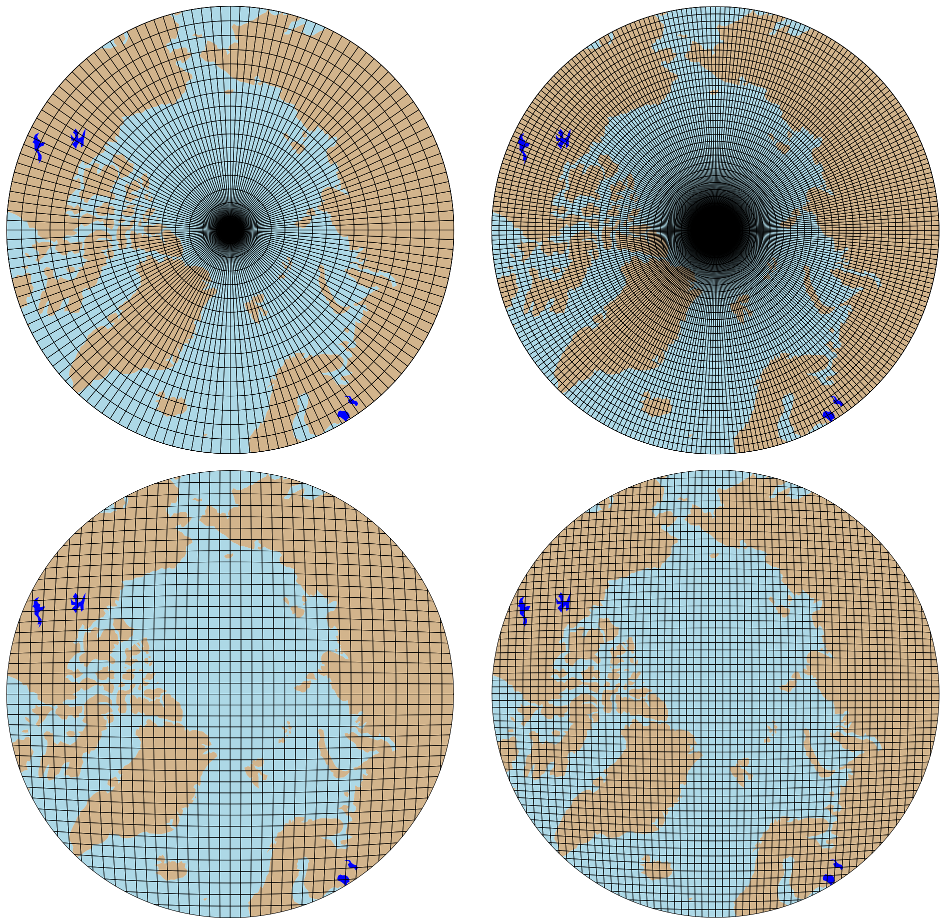

Figure 1. .

2.1.2 Spectral-element (SE) dynamical core

The SE dycore is a hydrostatic model that integrates the equations of motion using a high-order continuous Galerkin method (Taylor et al., 1997; Dennis et al., 2012). The computational domain is a cubed-sphere grid tiled with quadrilateral elements (e.g., Figure 2). Each element contains a fourth order basis set in each horizontal direction, with the solution defined at the roots of the basis functions, the Gauss-Lobatto-Legendre (GLL) quadrature points. This results in 16 GLL nodal points within each element, with 12 of the points lying on the (shared) element boundary. Communication between elements happens via the direct stiffness summation (Canuto et al., 2007), which applies a numerical flux to the element boundaries that reconciles overlapping nodal values and produces a continuous global basis set.

As with the FV dycore, the dynamics evolve in floating Lagrangian layers that are subsequently mapped to an Eulerian reference grid. A dry mass vertical coordinate was more recently implemented for thermodynamic consistency with condensates (Lauritzen et al., 2018). The 2D dynamics have no implicit dissipation and so hyperviscosity operators are applied to all prognostic variables to remove spurious numerical errors (Dennis et al., 2012). Laplacian damping is applied in the sponge layer.

The SE dycore supports regional grid refinement via its variable-resolution configuration, requiring two enhancements over uniform resolution grids. (1) As the numer-

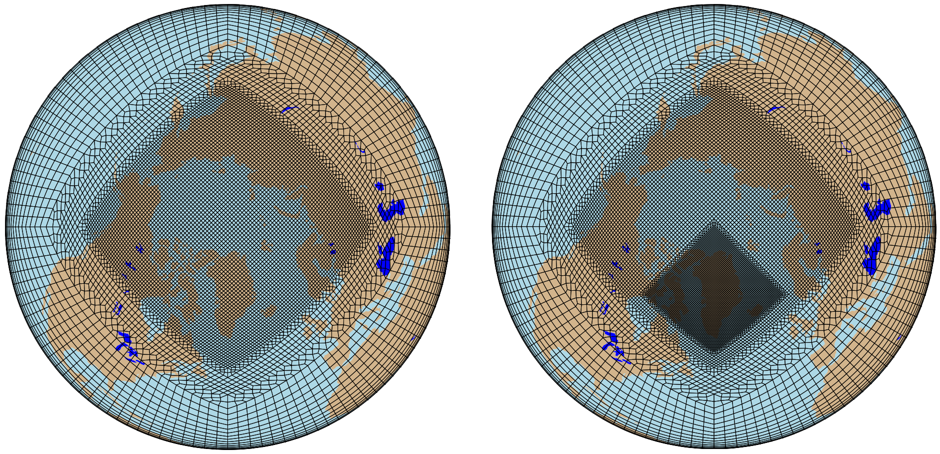

Figure 2. .

ical viscosity increases with resolution, explicit hyperviscosity relaxes according to the local element size, reducing in strength by about an order of magnitude per halving of the grid spacing. A tensor-hyperviscosity formulation is used (Guba et al., 2014), which adjusts the coefficients in two orthogonal directions to more accurately target highly distorted quadrilateral elements. (2) The topography boundary conditions need to be smoothed in a way that does not excite grid scale modes, and so the NCAR topography software (Lauritzen et al., 2015) was modified to scale the smoothing radius by the local element size.

For spectral-element grids with quasi-uniform grid spacing, a variant in which tracer advection is computed using the Conservative Semi-Lagrangian Multi-tracer transport scheme (CSLAM) is used instead (Lauritzen et al., 2017). CSLAM has improved tracer property preservation and accelerated multi-tracer transport. It uses a separate grid from the spectral-element dynamics, through dividing each element into 3×3 control volumes with quasi-equal area. The physical parameterizations are computed from the state on the CSLAM grid, which has clear advantages over the default SE dycore in which the physics are evaluated at the GLL nodal points (A. Herrington et al., 2018).

2.2 Grids

Six grid are evaluated in this study (Table X). The FV dycore is run with 1° and 2° grid spacing, referred to as $f09$ and $f19$, respectively (Figure 1a,b). The 1° equivalent of the CAM-SE-CSLAM grid is also run, referred to as $ne30pg3$ (Figure 1c), where ne refers to a grid with of $ne \times ne$ elements per cubed-sphere face, and pg denotes that there are $pg \times pg$ control volumes per element for computing the physics. An additional 1° CAM-SE-CSLAM grid is run, but with the physical paramerizations computed on a grid that contains 2×2 control volumes per element, $ne30pg2$ (Figure 1d; A. R. Herrington et al., 2019).

Two variable resolution meshes were developed as part of the CESM2.2 release that contains grid refinement over the Arctic (Figure 2). The Arctic meshes were developed using the software package SQuadgen (`https://github.com/ClimateGlobalChange/squadgen`). The $ARCTIC$ grid is a 1° grid with $\frac{1}{4}^{\circ}$ regional refinement over the broader Arctic region. The $ARCTICGRIS$ grid is identical to the $ARCTIC$ grid, but contains an additional patch covering the big island of Greenland with $\frac{1}{8}^{\circ}$ resolution.

2.3 Physical parameterizations

The CAM6 physical parameterization package (hereafter referred to as the *physics*; `https://ncar.github.io/CAM/doc/build/html/index.html`) is used for all simulations in this study. CAM6 physics is most noteably different from it's predecessors through the incorporation of high-order turbulence closure, Cloud Layers Unified by Binormals (CLUBB; Golaz et al., 2002; Bogenschutz et al., 2013), which jointly acts as a PBL, shallow convection and cloud macrophysics scheme. CLUBB is coupled with the MG2 microphysics scheme (Gettelman et al., 2015), with prognostic precipitation and classical nucleation theory in representing cloud ice for improved cloud-aerosol interactions. Deep convection is parameterized using a convective quasi-equilibrium mass flux scheme (Zhang & McFarlane, 1995; Neale et al., 2008) inlcuding convective momentum transport (Richter et al., 2010). PBL form drag is modeled after (Beljaars et al., 2004) and orographic gravity wave drag is represented with an anisotropic method informed by the orientation of topographic ridges at the sub-grid scale.

The CAM convention is that the physics package determines the vertical resolution. Since all runs use CAM6 physics, all grids and dycores use 32 levels in the vertical, with a model top of about 1 hPa or about 40 km. The physics time-step, in contrast, is dependent on grid resolution. Increases in horizontal resolution permit faster vertical velocities that reduce characteristic time-scales, and so the physics time-step should be reduced to avoid large time truncation errors (A. Herrington & Reed, 2018). The $ARCTIC$ and $ARCTICGRIS$ grids are therefore run with a 4× and 8× reduction in physics time-step relative to the default 1800 s time-step used in coarser, uniform resolution grids.

2.4 Experimental design

All grids and dycores are run using an identical transient 1979-1998 AMIP-style configuration, with prescribed monthly SST/sea-ice after (Hurrell et al., 2008). This configuration refers to the $FHIST$ *compset* and runs out of the box in CESM2.2. The Community Land Model (CLM5; `https://escomp.github.io/ctsm-docs/versions/release-clm5.0/html/users_guide/index.html`), which uses the same grid as the atmosphere grid, calculates the surface energy balance at each land tile within a grid cell, which is used to compute snow and bare ice melting to inform the surface mass balance (SMB) of a glacier unit (van Kampenhout et al., 2020). For land ice tiles coinciding with the Antarctic and Greenland Ice Sheets, the surface energy and mass balance are evaluated at ten elevation classes, and integrated over sub-grid hypsometric area-elevation bins for more accurate estimation of the surface mass balance of the big ice sheets. Ice accumulation is modeled as a capping flux, or snow in excess of the assumed 10 m snow cap, and refreezing of liquid within the snowpack additionally acts as a source of mass in the SMB calculation. Since the 10 m snowcap needs to be reached in the accumulation zone to simulate the SMB, the snow depths in the variable-resolution grids were spun-up by forcing CLM5 standalone, cycling over 20 years of a fully coupled $ARCTIC$ run for about 500 years. The uniform resolution grids are all initialized with an SMB from an existing $f09$ spun-up initial condition.

2.5 SMB Analysis

A common high resolution dataset is used to generate the GrIS boundary conditions using the CLM dataset creation tools. Since we are interested in the total ice sheet SMB, we seek to integrate various components of the SMB over a common ice mask to get the total mass change over the GrIS. Figure 7 shows the GrIS ice mask area across the different grids, as a function of the number of grid points. Due to the use conservative regridding in the CLM tools, the interpolation errors are small and ice mask areas have less than 1.5% errors relative to the raw ice mask dataset. RACMO, however, uses a smaller ice mask, about 3% smaller than the raw CLM dataset. While Figure 7 suggests integrating quantities over the native ice mask of the six grids would probably not suffer from large errors due to differing ice masks, we seek to compare these integrated quantities with RACMO. Therefore, we have taken the approach of mapping all model fields to the lowest resolution grids and integrating over the respective low resolution ice masks. Due to the sensitivity of mapping errors to grid coordinates (i.e., unstructured or structured), all quantities are evaluated on both the $f19$ and $ne30pg2$ low resolution grids. In addition, two remapping packages are used; ESMF conservative and a TempestRemap high-order, monotone algorithm. In all, each integrated quantity is evaluated (at most) four times to provide an estimate of uncertainty due to differences in grid coordinates and remapping algorithm.

3 Results

3.1 Tropospheric temperatures

Before delving into the simulated characteristics of the Arctic, the global mean differences between the grids and dycores are assessed, Figure 3 shows the climatological, zonal mean height plots expressed as differences between the uniform resolution grids and dycores. The $f09$ grid is warmer than the $f19$ grid, primarily in the mid-to-high latitudes and throughout the depth of the troposphere. This is a common response to increasing horizontal resolution in GCMs (Pope & Stratton, 2002; Roeckner et al., 2006), and (A. R. Herrington & Reed, 2020) has shown that this occurs in CAM due to greater resolved vertical velocities that in turn, facilitate greater condensational heating in the macrophyiscs routine in CLUBB. The right columns in Figure 3 supports this interpretation, which shows an increase in the climatological CLUBB heating in the mid-latitudes in the $f09$ grid.

As the SE dycore is less diffusive than the FV dycore, the resolved vertical velocities are larger in the SE dycore, and so a modest, resolution-like sensitivity occurs in which $ne30pg3$ is warmer than $f09$ (Figure 3). The stratosphere has a different response, in which $ne30pg3$ is much cooler than $f09$ in the mid-to-high latitudes. The differences in temperature between $ne30pg3$ and $ne30pg2$ are small, with a slight warming near the tropopause at high latitudes. This is consistent with the similar climates found between these grids in (A. R. Herrington et al., 2019).

Comparing the variable-resolution grids to the uniform resolution grids is complicated because we simultaneously increase the grid resolution and reduce the physics time-step, both which noticeably impact the solution (D. L. Williamson, 2008). An additional $ne30pg3$ simulations is run with the physics time-step used in the $ARCTIC$ grid, referred to as $ne30pg3^*$. Figure 4 shows the change in climatological temperature in zonal-mean height space between $ne30pg3^*$ and $ne30pg3$. A similar warming response to increasing resolution occurs when the time-step is reduced, and the mechanism is similar in that the shorter time-step facilitates greater condensational heating by CLUBB. Figure 4 shows the difference in climatological temperature between the $ARCTIC$ grid and the $ne30pg3^*$ grid. The greater condensational heating and warmer temperatures are confined to the regionally refined region when the impact of physics time-steps is removed from the analysis.

3.2 Synoptic-scale storm characteristics

Synoptic storms are identified and analyzed using TempestExtremes (Ullrich et al., 2021). The new $ARCTIC$ grid contains $\frac{1}{4}^\circ$ refinement north of about 45° latitude, and so the storm tracker is applied to this region for the $ARCTIC$ and $ne30pg3$ run to identify differences in storm characteristics due to horizontal resolution. Figure 5 shows the mean precipitation rates averaged over all January storms identified by TempestExtremes. The iconic comma structure of the mid-latitude cyclones is simulated in $ne30pg3$ and

$ARCTIC$ grids, with the magnitudes about the same in these two grids, with perhaps a marginal increase in precipitation rates in the storm center of the $ARCTIC$ grid. For good measure, the $ne30pg3^*$ run is also plotted, and looks more-or-less identical to the $ne30pg3$ run.

As has been previously reported, horizontal resolution can have large impacts on extreme precipitation events. Figure 6 is a PDF of the precipitation rates associated with synoptic storms, by month. The $ARCTIC$ run has larger extreme precipitation rates compared to $ne30pg3$ in every month, but the increase is greatest in the summer months, which coincides with the most extreme events of the year. This is primarily due to an increase in resolution; the $ne30pg3^*$ only marginally increases the precipitation rates compared with $ne30pg3$. The $f09$ and $f19$ grids looks similar to $ne30pg3$, but with $f09$ having more frequent extreme precipitation events than $f19$ (not shown). It should also be noted that the PDFs are evaluated on an identical composite grid for all runs, and so storm statistics are not impacted by differences in output resolution.

The extreme precipitation rates in the $ARCTIC$ run are closer to the ERA5 reanalysis than in $ne30pg3$ (Figure 6). It's difficult to know the extent that the extreme precipitation rates in ERA5 are constrained by data assimilation, or whether these precipitation rates are due to using a similar $\frac{1}{4}^\circ$ model as the $ARCTIC$ grid. However, precipitation rates in $\frac{1}{4}^\circ$ models tend to produce more skillful extreme events (O'Brien et al., 2016).

3.3 Orographic gravity waves emanating from Greenland

3.4 Katabatic winds emanating from Greenland

3.5 Greenland surface mass balance

The surface mass balance (SMB) of the Greenland Ice Sheet (GrIS) is simulated in all grids and dycores in this study. As the accuracy of the computed SMB is sensitive to grid resolution, Figure 7 shows the average grid spacing for all six grids in this study. The $ne30pg2$ grid has the coarsest representation with an average $\Delta x = 160\ km$, and the $ARCTICGRIS$ grid has the highest resolution with an average $\Delta x = 14.6\ km$, similar to the grid spacing of the 11 km RACMO model. The $ne30pg3$ grid has an average $\Delta x = 111.2\ km$, which is substantially more coarse than the $f09$ grid, having an average $\Delta x = 60\ km$. This is interesting because $ne30pg3$ and $f09$ have similar average grid spacing over the entire globe, and comparable computational costs, but due to the convergence of meridians the finite-volume model has enhanced resolution over GrIS. The $ARCTIC$ grid has an average grid spacing over GrIS of $\Delta x = 27.8\ km$, and is about 10 times more expensive than the 1° models. The $ARCTICGRIS$ grid is about twice as expensive as the $ARCTIC$ grid.

4 Conclusions

Acknowledgments

This material is based upon work supported by the National Center for Atmospheric Research (NCAR), which is a major facility sponsored by the NSF under Cooperative Agreement 1852977. Computing and data storage resources, including the Cheyenne supercomputer (doi:10.5065/D6RX99HX), were provided by the Computational and Information Systems Laboratory (CISL) at NCAR.

The data presented in this manuscript is available at `https://github.com/adamrher/2020-arcticgrids`.

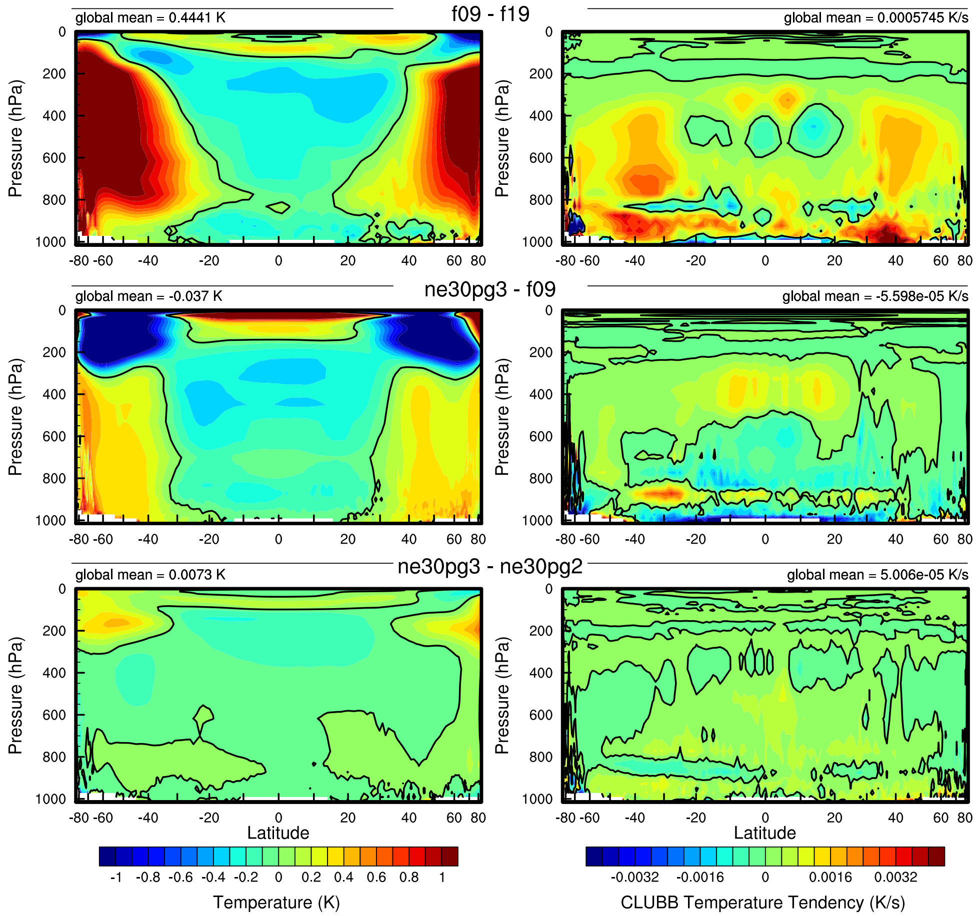

Figure 3. .

References

Beljaars, A., Brown, A., & Wood, N. (2004). A new parametrization of turbulent orographic form drag. *Quart. J. Roy. Meteor. Soc.*, *130*(599), 1327–1347. doi: 10.1256/qj.03.73

Bogenschutz, P. A., Gettelman, A., Morrison, H., Larson, V. E., Craig, C., & Schanen, D. P. (2013). Higher-order turbulence closure and its impact on climate simulations in the community atmosphere model. *Journal of Climate*, *26*(23), 9655–9676.

Bromwich, D. H., Cassano, J. J., Klein, T., Heinemann, G., Hines, K. M., Steffen, K., & Box, J. E. (2001). Mesoscale modeling of katabatic winds over greenland with the polar mm5. *Monthly Weather Review*, *129*(9), 2290–2309.

Canuto, C., Hussaini, M. Y., Quarteroni, A., & Zang, T. (2007). *Spectral methods: Evolution to complex geometries and applications to fluid dynamics* (1st ed.). Springer.

Collins, W. D., Rasch, P. J., Boville, B. A., Hack, J. J., McCaa, J. R., Williamson, D. L., ... Zhang, M. (2006). The formulation and atmospheric simulation of the community atmosphere model version 3 (cam3). *Journal of Climate*, *19*(11), 2144–2161.

Dennis, J. M., Edwards, J., Evans, K. J., Guba, O., Lauritzen, P. H., Mirin, A. A., ... Worley, P. H. (2012). CAM-SE: A scalable spectral element dynamical

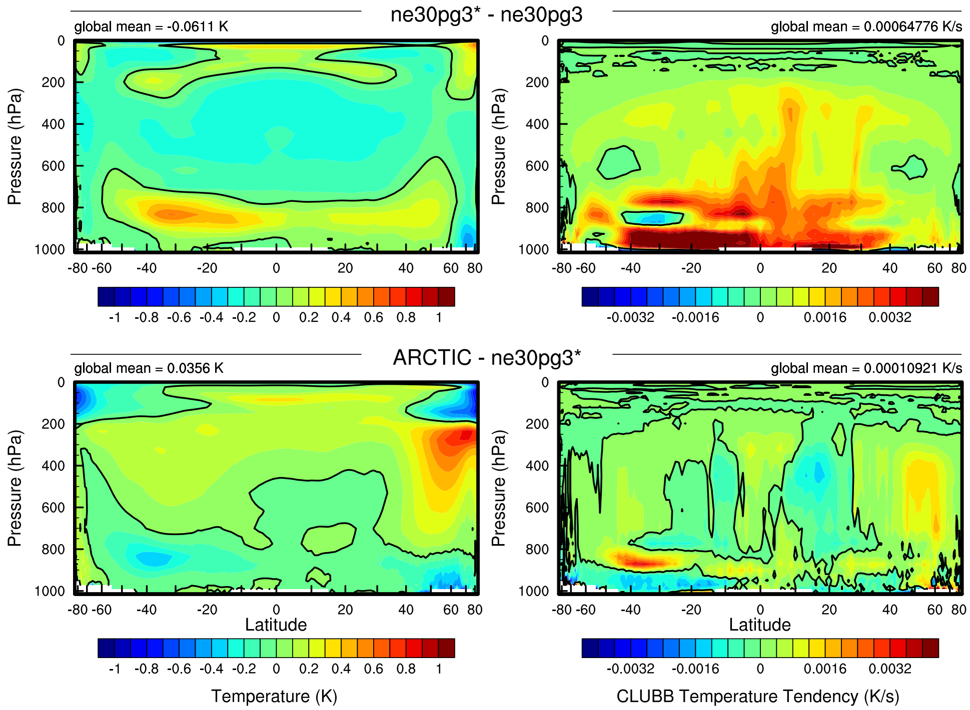

Figure 4. .

core for the Community Atmosphere Model. *Int. J. High. Perform. C.*, *26*(1), 74-89. Retrieved from `http://hpc.sagepub.com/content/26/1/74.abstract` doi: 10.1177/1094342011428142

Gettelman, A., Morrison, H., Santos, S., Bogenschutz, P., & Caldwell, P. (2015). Advanced two-moment bulk microphysics for global models. part ii: Global model solutions and aerosol–cloud interactions. *Journal of Climate*, *28*(3), 1288–1307.

Golaz, J.-C., Larson, V. E., & Cotton, W. R. (2002). A pdf-based model for boundary layer clouds. part i: Method and model description. *Journal of the Atmospheric Sciences*, *59*(24), 3540–3551. doi: 10.1175/1520-0469(2002)059⟨3540:apbmfb⟩2.0.co;2

Guba, O., Taylor, M. A., Ullrich, P. A., Overfelt, J. R., & Levy, M. N. (2014). The spectral element method (sem) on variable-resolution grids: evaluating grid sensitivity and resolution-aware numerical viscosity. *Geosci. Model Dev.*, *7*(6), 2803–2816. doi: 10.5194/gmd-7-2803-2014

Herrington, A., Lauritzen, P., Taylor, M. A., Goldhaber, S., Eaton, B. E., Bacmeister, J., . . . Ullrich, P. (2018). Physics-dynamics coupling with element-based high-order galerkin methods: quasi equal-area physics grid. *Mon. Wea. Rev.*, *47*, 69–84. doi: 10.1175/MWR-D-18-0136.1

Herrington, A., & Reed, K. (2018). An idealized test of the response of the community atmosphere model to near-grid-scale forcing across hydrostatic resolutions. *J. Adv. Model. Earth Syst.*, *10*(2), 560–575.

Herrington, A. R., Lauritzen, P. H., Reed, K. A., Goldhaber, S., & Eaton, B. E. (2019). Exploring a lower resolution physics grid in cam-se-cslam. *Journal of Advances in Modeling Earth Systems*, *11*.

Herrington, A. R., & Reed, K. A. (2020). On resolution sensitivity in the community atmosphere model. *Quarterly Journal of the Royal Meteorological Society*,

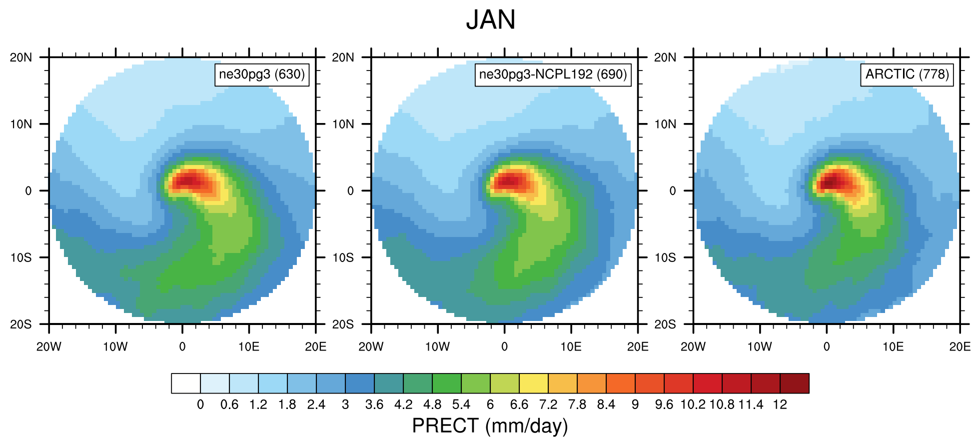

Figure 5. .

146(733), 3789–3807.

Hurrell, J. W., Hack, J. J., Shea, D., Caron, J. M., & Rosinski, J. (2008). A new sea surface temperature and sea ice boundary dataset for the community atmosphere model. *Journal of Climate*, *21*(19), 5145–5153.

Jablonowski, C., & Williamson, D. L. (2006). A baroclinic instability test case for atmospheric model dynamical cores. *Q. J. R. Meteorol. Soc.*, *132*, 2943-2975.

Jablonowski, C., & Williamson, D. L. (2011). The pros and cons of diffusion, filters and fixers in atmospheric general circulation models., in: P.H. Lauritzen, R.D. Nair, C. Jablonowski, M. Taylor (Eds.), Numerical techniques for global atmospheric models. *Lecture Notes in Computational Science and Engineering, Springer*, *80*.

Lauritzen, P. H., Bacmeister, J. T., Callaghan, P. F., & Taylor, M. A. (2015). Ncar global model topography generation software for unstructured grids. *Geoscientific Model Development Discussions*, *8*(6), 4623–4651. doi: 10.5194/gmdd-8-4623-2015

Lauritzen, P. H., Mirin, A., Truesdale, J., Raeder, K., Anderson, J., Bacmeister, J., & Neale, R. B. (2011). Implementation of new diffusion/filtering operators in the CAM-FV dynamical core. *Int. J. High Perform. Comput. Appl.*. doi: 10.1177/1094342011410088

Lauritzen, P. H., Nair, R., Herrington, A., Callaghan, P., Goldhaber, S., Dennis, J., … Dubos, T. (2018). NCAR CESM2.0 release of CAM-SE: A reformulation of the spectral-element dynamical core in dry-mass vertical coordinates with comprehensive treatment of condensates and energy. *J. Adv. Model. Earth Syst.*. doi: 10.1029/2017MS001257

Lauritzen, P. H., Taylor, M. A., Overfelt, J., Ullrich, P. A., Nair, R. D., Goldhaber, S., & Kelly, R. (2017). CAM-SE-CSLAM: Consistent coupling of a conservative semi-lagrangian finite-volume method with spectral element dynamics. *Mon. Wea. Rev.*, *145*(3), 833-855. doi: 10.1175/MWR-D-16-0258.1

Lin, S.-J. (2004). A 'vertically Lagrangian' finite-volume dynamical core for global models. *Mon. Wea. Rev.*, *132*, 2293-2307.

Lin, S.-J., & Rood, R. B. (1997). An explicit flux-form semi-Lagrangian shallow-water model on the sphere. *Q.J.R.Meteorol.Soc.*, *123*, 2477-2498.

Lofverstrom, M., Fyke, J. G., Thayer-Calder, K., Muntjewerf, L., Vizcaino, M., Sacks, W. J., … Bradley, S. L. (2020). An efficient ice sheet/earth system model spin-up procedure for cesm2-cism2: Description, evaluation, and broader applicability. *Journal of Advances in Modeling Earth Systems*, *12*(8),

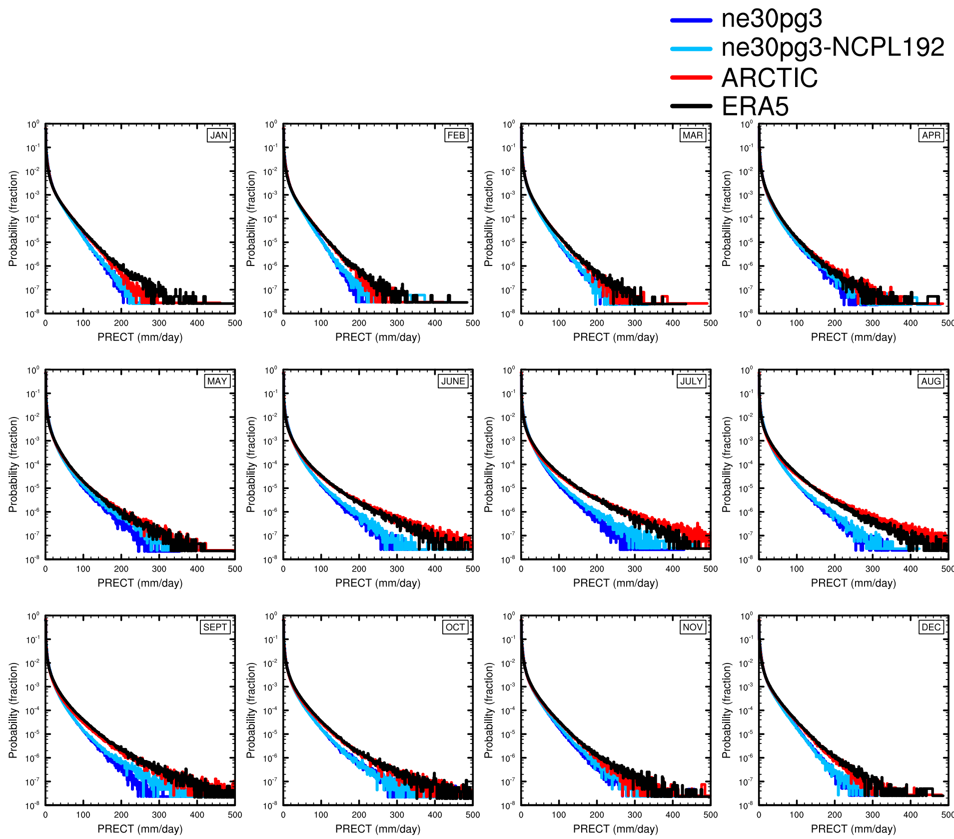

Figure 6. .

e2019MS001984.

Neale, R. B., Richter, J. H., & Jochum, M. (2008). The impact of convection on ENSO: From a delayed oscillator to a series of events. *J. Climate*, *21*, 5904-5924.

Noël, B., van de Berg, W. J., Lhermitte, S., & van den Broeke, M. R. (2019). Rapid ablation zone expansion amplifies north greenland mass loss. *Science advances*, *5*(9), eaaw0123.

O'Brien, T. A., Collins, W. D., Kashinath, K., Rübel, O., Byna, S., Gu, J., … Ullrich, P. A. (2016). Resolution dependence of precipitation statistical fidelity in hindcast simulations. *J. Adv. Model. Earth Syst.*, *8*(2), 976–990. Retrieved from `http://dx.doi.org/10.1002/2016ms000671` doi: 10.1002/2016ms000671

Pope, V., & Stratton, R. (2002). The processes governing horizontal resolution sensitivity in a climate model. *Climate Dynamics*, *19*(3-4), 211–236.

Putman, W. M., & Lin, S.-J. (2007). Finite-volume transport on various cubed-sphere grids. *J. Comput. Phys.*, *227*(1), 55-78.

Richter, J. H., Sassi, F., & Garcia, R. R. (2010). Toward a physically based gravity wave source parameterization in a general circulation model. *J. Atmos. Sci.*, *67*, 136-156. doi: dx.doi.org/10.1175/2009JAS3112.1

Roeckner, E., Brokopf, R., Esch, M., Giorgetta, M., Hagemann, S., Kornblueh, L., … Schulzweida, U. (2006). Sensitivity of simulated climate to horizontal and vertical resolution in the echam5 atmosphere model. *Journal of Climate*, *19*(16), 3771–3791.

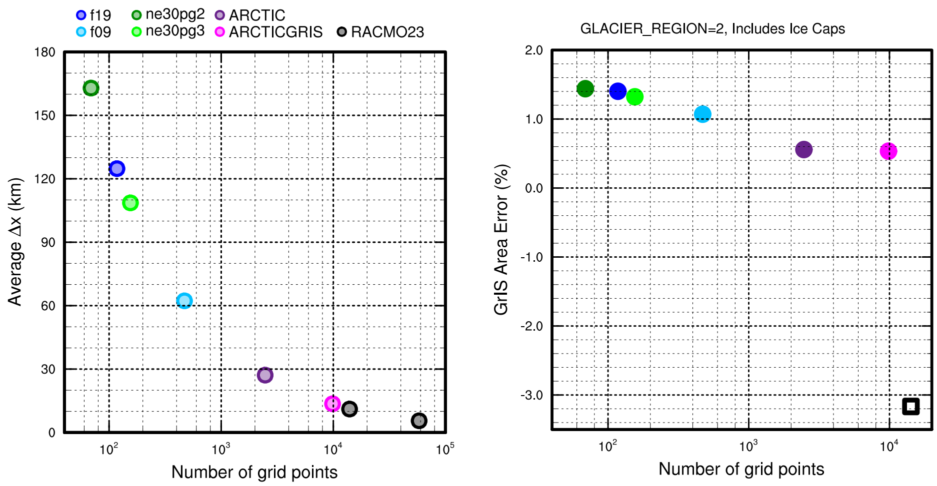

Figure 7. .

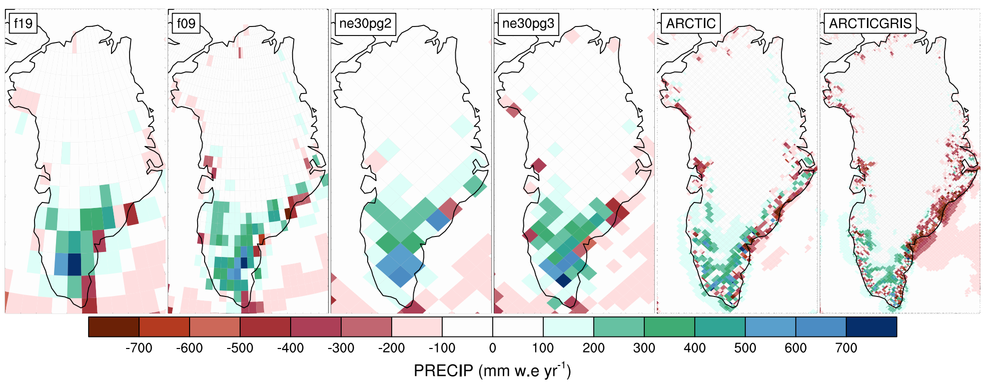

Figure 8. Climatological (1979-1998) annual precipitation rate bias relative to the RACMO2.3p2 5.5km resolution data product (Noël et al., 2019).

Smirnova, J., & Golubkin, P. (2017). Comparing polar lows in atmospheric reanalyses: Arctic system reanalysis versus era-interim. *Monthly Weather Review*, *145* (6), 2375–2383.

Stocker, T. (2014). *Climate change 2013: the physical science basis: Working group i contribution to the fifth assessment report of the intergovernmental panel on climate change*. Cambridge university press.

Suarez, M. J., & Takacs, L. L. (1995). Volume 5 documentation of the aries/geos dynamical core: Version 2.

Taylor, M. A., Tribbia, J., & Iskandarani, M. (1997). The spectral element method for the shallow water equations on the sphere. *J. Comput. Phys.*, *130*, 92-108.

Ullrich, P. A., Zarzycki, C. M., McClenny, E. E., Pinheiro, M. C., Stansfield, A. M., & Reed, K. A. (2021). Tempestextremes v2. 1: a community framework for feature detection, tracking and analysis in large datasets. *Geoscientific Model Development Discussions*, 1–37.

van Kampenhout, L., Lenaerts, J. T., Lipscomb, W. H., Lhermitte, S., Noël, B., Vizcaíno, M., . . . van den Broeke, M. R. (2020). Present-day greenland ice sheet climate and surface mass balance in cesm2. *Journal of Geophysical Research: Earth Surface*, *125* (2), e2019JF005318.

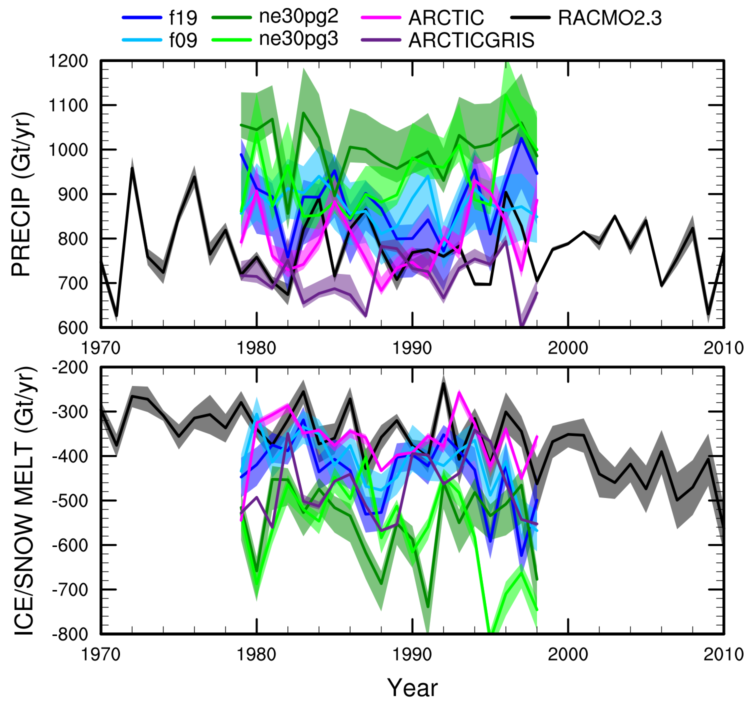

Figure 9. Time-series of annual (solid+liquid) precipitation (top) and annual runoff (bottom) integrated over the Greenland Ice Sheet for all six simulations and compared to RACMO3.2. The raw fields are mapped to two target low resolution grids, f19 & ne30pg2, and using two different remapping methods, conservative ESMF and high order TempestRemap. The remapped values are then integrated over the ice mask of the target grid. This gives four time-series for each simulation (three for f19 & ne30pg2), with the mean value given by the solid line and shading spanning the extent of the remapped solutions.

van Kampenhout, L., Rhoades, A. M., Herrington, A. R., Zarzycki, C. M., Lenaerts, J. T. M., Sacks, W. J., & van den Broeke, M. R. (2018). Regional grid refinement in an earth system model: Impacts on the simulated greenland surface mass balance. *The Cryosphere Discuss.*. doi: 10.5194/tc-2018-257

Williamson, D. (2007). The evolution of dynamical cores for global atmospheric models. *J. Meteor. Soc. Japan*, *85*, 241-269.

Williamson, D. L. (2008). Convergence of aqua-planet simulations with increasing resolution in the community atmospheric model, version 3. *Tellus A*, *60*(5), 848–862. doi: 10.1111/j.1600-0870.2008.00339.x

Zhang, G., & McFarlane, N. (1995). Sensitivity of climate simulations to the parameterization of cumulus convection in the canadian climate centre general circulation model. *Atmosphere-ocean*, *33*(3), 407-446.

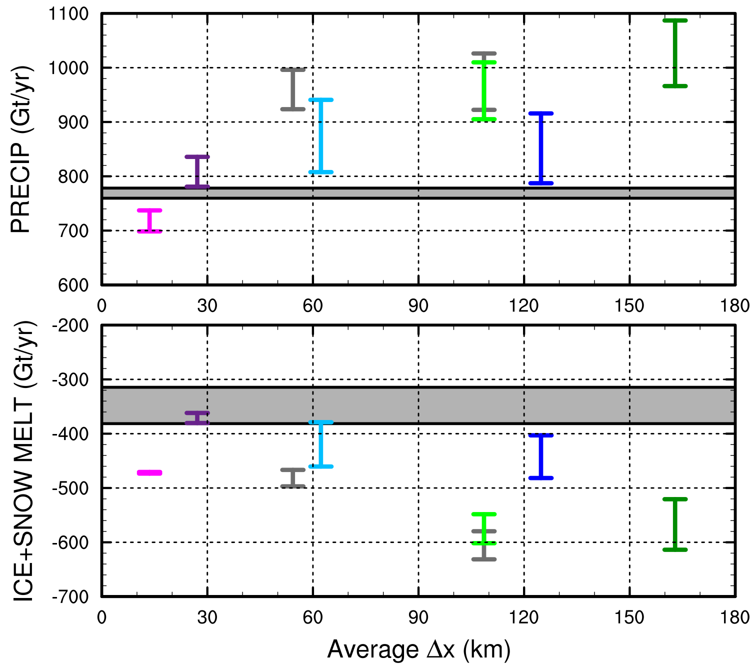

Figure 10. .

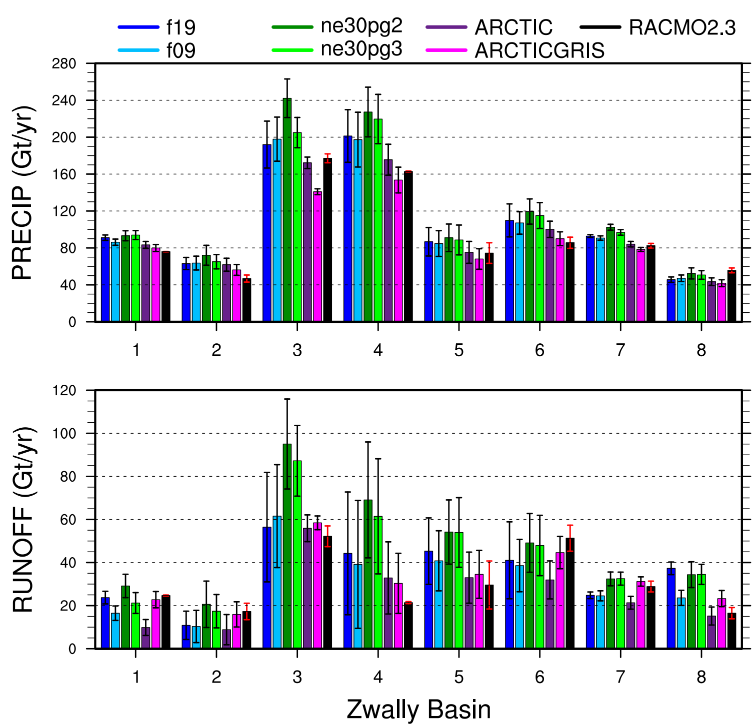

Figure 11. .

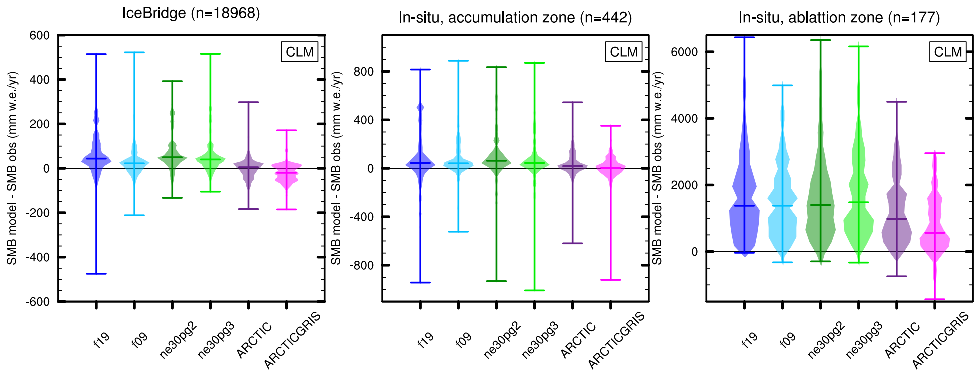

Figure 12. .

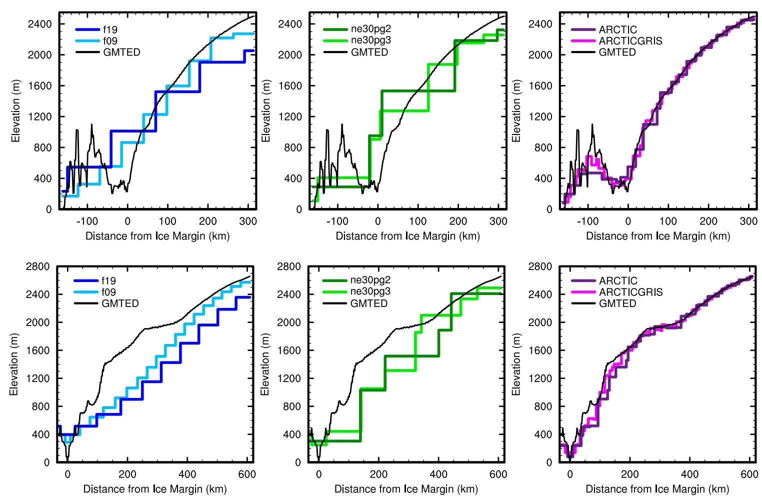

Figure 13. .

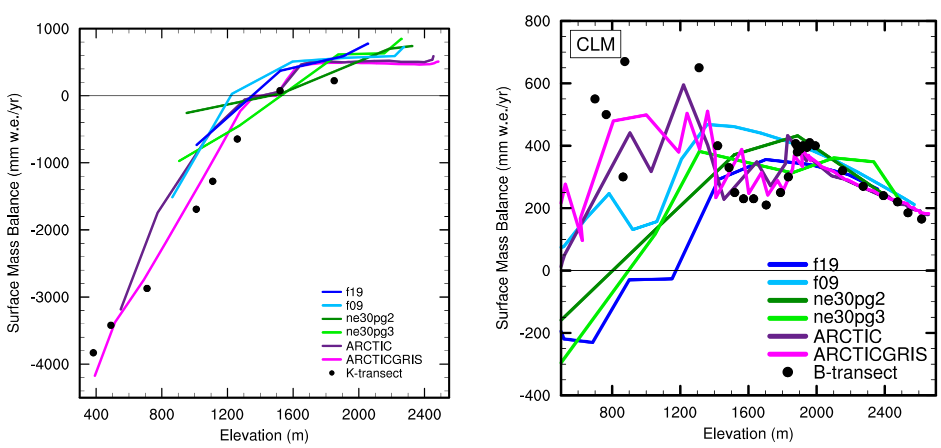

Figure 14. .